INTERNATIONAL JOURNAL FOR NUMERICAL METHODS IN FLUIDS
Int. J. Numer. Meth. Fluids 2003; **42**:641–663 (DOI: 10.1002/fld.539)

Numerical wave tank based on a σ-transformed finite element inviscid flow solver

M. S. Turnbull[1], A. G. L. Borthwick[2,*,†] and R. Eatock Taylor[2]

[1]*HR Wallingford Ltd, Howbery Park, Wallingford, Oxon OX10 8BA, U.K.*
[2]*Department of Engineering Science, University of Oxford, Parks Road, Oxford, U.K.*

SUMMARY

Inviscid two-dimensional free surface wave motions are simulated using a σ-transformed finite-element model based on potential theory for irrotational, incompressible fluid flow over a flat fixed bed. The free surface boundary condition is fully non-linear, and so non-linear effects up to very high order can be modelled. The σ-transformation involves linear stretching of the mesh between the bed and free surface. This has two major advantages. First, remeshing due to the moving free surface is avoided. Second, the mesh nodes are aligned vertically, allowing a high order calculation of the free surface vertical velocity component to be implemented without smoothing, except for very steep waves. The model however is further restricted to non-overturning, non-breaking waves because of the uniqueness of the σ-transformation. Excellent agreement is obtained with analytical and alternative numerical data for small amplitude free sloshing in a rectangular tank and forced sloshing in a horizontally base-excited rectangular tank. At higher amplitudes, non-linear effects are evident in the simulations by the present numerical model. The model is also able to reproduce steep progressive waves due to a wave-maker in agreement with Stokes 5th theory, second-order shallow water waves in agreement with cnoidal theory, and focused wave groups that match the experimental measurements acquired by Baldock *et al.* [A laboratory study of non-linear surface waves on water. *Phil. Trans. R. Soc. Lond. A* 1996; **354**:649–676]. Copyright © 2003 John Wiley & Sons, Ltd.

KEY WORDS: numerical wave tank; finite elements; steep waves

1. INTRODUCTION

An understanding of non-linear free surface motions is important in many engineering liquid–structure interaction problems. The ringing of offshore structures interacting with steep waves is believed to be a phenomenon driven by high-order non-linear behaviour of the free surface (see e.g. Grue *et al.* [1], Faltinsen *et al.* [2], Stansberg *et al.* [3], Chaplin *et al.* [4]). Ringing

*Correspondence to: A. G. L. Borthwick, Department of Engineering Science, University of Oxford, Parks Road, Oxford OX1 3PJ, U.K.
†E-mail: alistair.borthwick@eng.ox.ac.uk

Contract/grant sponsor: Engineering and Physical Sciences Research Council (EPSRC)

Received 17 April 2002
Revised 16 February 2003

exhibits itself as a transient high frequency oscillatory structural response and is particularly relevant to floating structures containing large diameter vertical columns, such as tension leg and gravity platforms. Inundation and non-linear sloshing of greenwater on the decks of vessels is also due to interactions with steep waves. Furthermore, large amplitude sloshing effects within containers (e.g. oil storage cylinders) can seriously impair structural integrity after an earthquake has occurred.

Steep gravity waves are, by definition, non-linear due to the non-linear dynamic and kinematic free surface boundary conditions, themselves specified on the unknown position of the free surface. The governing equations are usually posed with the assumptions of an inviscid and incompressible liquid. Low order perturbation techniques can be used to obtain analytical solutions for mildly non-linear problems, but outside their range of validity it is necessary to resort to numerical methods. Such methods for simulating waves may then be readily extended to model the interaction of waves and fixed or moving bodies on or beneath the free surface. To date the most common numerical approach has been the boundary element method. Longuet-Higgins and Cokelet [5] were the first to use this approach to model fully non-linear wave problems in the time domain. The early work was directed at an understanding of steep waves in the absence of bodies, and assumed periodicity of the propagating waves. More recently, the full non-linear diffraction-radiation problem in steep transient waves has been investigated using the boundary element method. A comprehensive survey of the application of boundary element techniques to numerical wave tanks has been provided in the review by Kim *et al.* [6]. In subsequent work, Ferrant [7] has shown how both waves and currents may be included in the model, and Boo [8] has illustrated the advantages of using higher order boundary elements.

The review by Kim *et al.* [6] did not attempt to cover the progress being made in using the finite element method as the basis for a numerical wave tank. Wu and Eatock Taylor [9] used this approach for fully non-linear problems in two dimensions. A comparison of the boundary element and finite element methods for the non-linear wave–body interaction problem was made by Wu and Eatock Taylor [10]. This suggested that the finite element method could be more efficient than the boundary element method if one could exploit the banded structure of the resulting finite element equations. The approach was subsequently developed for a three-dimensional tank by Wu *et al.* [11] and Ma *et al.* [12, 13]. The latter work led to some good comparisons with physical model tests in steep waves conducted by Nestegard [14].

Other research is being conducted on alternative modelling strategies for a numerical wave tank, and on improvements to the finite element approach which would increase its efficiency and robustness. Robertson and Sherwin [15] have adopted an hp/spectral element model. Chern *et al.* [16, 17] used a pseudo-spectral collocation method for both two-dimensional and three-dimensional problems and this approach has been developed further by Le Touzé *et al.* [18]. A hybrid method, which aims to capture the advantages of both boundary element and finite element equation structure, has recently been developed by Wu and Eatock Taylor [19]. Boundary elements are used in a regime close to the body, and a structural finite element mesh away from it. This is related to the idea explored here of coupling an unstructured finite element mesh around the body with a simple structured mesh in the outer domain. Because a large spatial domain may need to be included in the modelling of a numerical wave tank, to avoid problems arising from reflections off the body, it is advantageous to employ a simple structured mesh in regions distant from the body. Significant additional savings could be achieved if it were possible to avoid remeshing in the outer domain as the flow evolves.

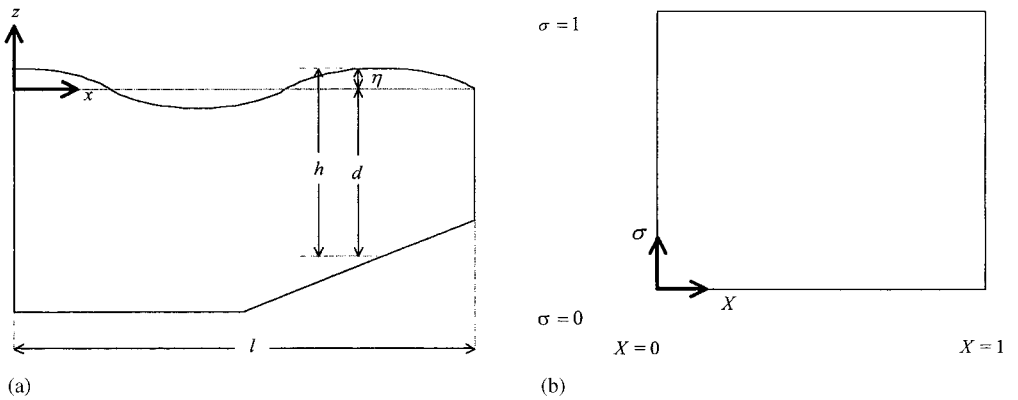

Figure 1. (a) Physical domain, (b) Computational domain.

The present paper aims to demonstrate the feasibility of solving the fully non-linear problem using the finite-element method, but without remeshing. It is based on an extended version of the two-dimensional finite element model developed by Wu and Eatock Taylor [9, 10] who used a structured mesh that was regenerated each time step to fit the moving free surface. In the present model, a sigma-transform is used to map the physical mesh linearly between the bed and free surface onto a fixed computational mesh. Similar mappings have previously been used by Stelling and Van Kester [20], Huang and Spaulding [21], and Koçyigit *et al.* [22] for shallow flows, and in a pseudo-spectral element approach for inviscid wave motions described by Chern *et al.* [16]. The present model is used to predict non-linear wave sloshing in a tank, steep regular wave profiles and focused wave groups in a flume. Free surface smoothing was only required for steep progressive waves. The following sections first introduce the governing equations, the sigma-transformed finite element formulation, and then give results from a series of validation tests.

2. GOVERNING EQUATIONS

Figure 1(a) depicts a Cartesian co-ordinate system O-*xz* such that the origin is on the mean free surface and z is vertically upwards. The fluid is assumed to be inviscid and incompressible, and the flow irrotational. Hence a velocity potential ϕ exists which satisfies Laplace's equation,

$$\nabla^2\phi = 0 \tag{1}$$

The velocity is specified at tank walls, and at the wave-maker, where required. The boundary condition on the velocity boundary (e.g. the wave-maker) is,

$$\frac{\partial\phi}{\partial n} = f_2 \tag{2}$$

where f_2 is the normal velocity at the boundary and n is normal to the boundary and is directed out of the fluid domain.

On the free surface, the two-dimensional non-linear dynamic and kinematic free surface boundary conditions are to be satisfied. These are:

$$g\eta + \frac{\partial \phi}{\partial t} + \frac{1}{2}\nabla\phi \cdot \nabla\phi = 0 \tag{3}$$

and

$$\frac{\partial \phi}{\partial z} = \frac{\partial \eta}{\partial t} + \frac{\partial \phi}{\partial x}\frac{\partial \eta}{\partial x} \tag{4}$$

where η is the free surface elevation vertically above the still water level, g is the acceleration due to gravity and t is time. The dynamic free surface boundary condition comes from Bernoulli's equation with relative pressure equal to zero. The kinematic condition is effectively a statement that particles on the free surface remain on the free surface.

In the case of a long flume, a condition is imposed in the vicinity of the downstream end, to absorb the incoming waves without causing reflections. This is discussed further below.

3. σ-TRANSFORMED FINITE ELEMENT FORMULATION

3.1. Computational domain

A triangular finite element mesh is used to discretize the flow domain. Assuming that the liquid is uniquely connected in the vertical direction, a linear stretching can be applied to map the mesh from the physical (wavy) domain to a σ-transformed computational domain on which the finite element computations are performed. This eliminates the need for remeshing according to the position of the free surface as would be undertaken in arbitrary Lagrange–Eulerian finite element schemes for example. Moreover, the resulting mesh is structured, with triangular element nodes lying along vertical lines, thus enabling the higher-order velocity calculation described in Section 3.4.2 to be used to update the vertical component of the surface velocity.

3.2. σ-transformation

The transformation from the physical (x, z, t) to the σ-transformed (X, σ, T) system is based on the following mappings:

$$X = \frac{x}{l}, \quad \sigma = \frac{z+d}{h} \quad \text{and} \quad T = t \tag{5}$$

where l is the length of the domain, d is the depth of the domain (the distance from the sea bed to the mean free surface) and h is the distance of the sea bed to the actual free surface (see Figure 1(a)). Using the chain rule, the derivative operators are:

$$\frac{\partial}{\partial x} = \frac{1}{l}\frac{\partial}{\partial X} + \left(\frac{\partial \sigma}{\partial x}\right)\frac{\partial}{\partial \sigma}, \quad \frac{\partial}{\partial z} = \frac{1}{h}\frac{\partial}{\partial \sigma} \quad \text{and} \quad \frac{\partial}{\partial t} = \frac{\partial}{\partial T} + \left(\frac{\partial \sigma}{\partial t}\right)\frac{\partial}{\partial \sigma} \tag{6}$$

The derivatives of σ with respect to x and t are found from

$$\frac{\partial \sigma}{\partial x} = \frac{1}{lh}\left(-\sigma\frac{\partial \eta}{\partial X} + (1-\sigma)\frac{\partial d}{\partial X}\right) \quad \text{and} \quad \frac{\partial \sigma}{\partial t} = \frac{1}{h}\left(-\sigma\frac{\partial \eta}{\partial T}\right) \tag{7}$$

where η is the free surface elevation measured from the mean free surface ($h=\eta+d$), and it is assumed that the mean depth is constant.

3.3. Finite element formulation

Using the Galerkin technique, Laplace's equation is multiplied by each shape function in turn and integrated over the entire domain (see Wu and Eatock Taylor [10]) to give:

$$\int_R \nabla N_i \cdot \sum_{j=1}^{n} \Phi_j \nabla N_j \, \mathrm{d}R|_{j\notin S_1} = -\int_R \nabla N_i \cdot \sum_{j=1}^{n} \Phi_j \nabla N_j \, \mathrm{d}R|_{j\in S_1} + \int_{S_2} N_i f_2 \, \mathrm{d}S \tag{8}$$

where n is the number of nodes, Φ_j is the nodal velocity potential and $N_j(X,\sigma)$ are the linear shape functions, S_1 and S_2 are the surfaces on which the potential and its normal derivative are specified, respectively, and R is the flow domain. The equation is written in matrix form, $[A]\{\Phi\}=\{B\}$ where $\{\Phi\}$ is the vector of the nodal velocity potentials and the coefficients of $[A]$ and $\{B\}$ are given by

$$A_{ij} = \int_R \nabla N_i \cdot \nabla N_j \, \mathrm{d}R \quad \text{or} \quad \begin{array}{ll} A_{ij}=1 & \text{if } i=j \text{ and } i\in S_1 \\ A_{ij}=0 & \text{if } (i\in S_1 \text{ or } j\in S_1) \text{ and } i\neq j \end{array} \tag{9}$$

and

$$B_i = -\sum_{j=1}^{n} \Phi_j \left(\int_R \nabla N_i \cdot \nabla N_j \, \mathrm{d}R \right)\Bigg|_{j\in s_1} + \int_{S_2} N_i f_2 \, \mathrm{d}S \quad \text{or} \quad B_i = \Phi_i \quad \text{if } i\in S_1 \tag{10}$$

The Jacobian of the transformation is

$$\frac{\partial(X,\sigma)}{\partial(x,z)} = \begin{vmatrix} \dfrac{\partial X}{\partial x} & \dfrac{\partial X}{\partial z} \\ \dfrac{\partial \sigma}{\partial x} & \dfrac{\partial \sigma}{\partial z} \end{vmatrix} = \begin{vmatrix} \dfrac{1}{l} & 0 \\ \dfrac{\partial \sigma}{\partial x} & \dfrac{1}{h} \end{vmatrix} = \frac{1}{lh} \tag{11}$$

and so

$$\mathrm{d}R = \mathrm{d}x \, \mathrm{d}z = lh \, \mathrm{d}X \, \mathrm{d}\sigma \tag{12}$$

The gradient operator can be expressed in terms of the transformed co-ordinates:

$$\nabla = \begin{pmatrix} \dfrac{\partial}{\partial x} \\ \dfrac{\partial}{\partial z} \end{pmatrix} = \begin{pmatrix} \dfrac{1}{l}\dfrac{\partial}{\partial X} + \left(\dfrac{\partial \sigma}{\partial x}\right)\dfrac{\partial}{\partial \sigma} \\ \dfrac{1}{h}\dfrac{\partial}{\partial \sigma} \end{pmatrix} \tag{13}$$

The spatial derivatives of the shape functions become:

$$\frac{\partial N_i}{\partial X} = \frac{\beta_i}{2\Delta} \quad \text{and} \quad \frac{\partial N_i}{\partial \sigma} = \frac{\gamma_i}{2\Delta} \tag{14}$$

Therefore, integrating $\nabla N_i \cdot \nabla N_j$ over one element (e) gives

$$\frac{1}{l}\frac{\beta_i\beta_j}{4\Delta^2}\int_e h\,\mathrm{d}X\,\mathrm{d}\sigma + \frac{\beta_i\gamma_j+\beta_j\gamma_i}{4\Delta^2}\int_e\left(\frac{\partial\sigma}{\partial x}\right)h\,\mathrm{d}X\,\mathrm{d}\sigma + \frac{l\gamma_i\gamma_j}{4\Delta^2}\int_e\left(\frac{\partial\sigma}{\partial x}\right)^2 h\,\mathrm{d}X\,\mathrm{d}\sigma + \frac{l\gamma_i\gamma_j}{4\Delta^2}\int_e\frac{1}{h}\,\mathrm{d}X\,\mathrm{d}\sigma \tag{15}$$

The coefficient A_{ij} is obtained by summing (15) over all elements. Provided the surface S_2 on which $\partial\Phi/\partial n$ is specified is vertical, the second term in (10) can be expressed as

$$\int_{S_2} N_i f_2\,\mathrm{d}S = \int_0^1 N_i f_2 h\,\mathrm{d}\sigma \tag{16}$$

The matrix equation is solved using Gaussian elimination.

3.4. *Velocity calculation*

Once the potential at all the nodes has been evaluated, the gradients of the potential in the X and σ directions are calculated. Two alternative methods of obtaining these gradients are described here.

3.4.1. The least squares method. Each node, P_j is connected to p other nodes by the finite element mesh. Let the position vector of the kth node relative to P_j be denoted by l^k. The X and σ components of l^k divided by the magnitude of l^k are written l_x^k and l_z^k. The least squares method involves solving the following matrix equation at each node P_j:

$$\begin{pmatrix} \sum_{k=1}^{P} l_X^k l_X^k & \sum_{k=1}^{P} l_X^k l_\sigma^k \\ \sum_{k=1}^{P} l_X^k l_\sigma^k & \sum_{k=1}^{P} l_\sigma^k l_\sigma^k \end{pmatrix} \begin{Bmatrix} \dfrac{\partial\Phi}{\partial X} \\ \dfrac{\partial\Phi}{\partial\sigma} \end{Bmatrix} = \begin{Bmatrix} \sum_{k=1}^{P} l_X^k \dfrac{\partial\Phi}{\partial l^k} \\ \sum_{k=1}^{P} l_\sigma^k \dfrac{\partial\Phi}{\partial l^k} \end{Bmatrix} \tag{17}$$

which yields the required gradient vector. This method is described by Eatock Taylor *et al.* [23] and is suitable for any kind of unstructured mesh.

3.4.2. Higher order calculation. For the structured meshes used in this paper, each node on the free surface will have a number of nodes vertically beneath it with the same X co-ordinate. This allows a better estimate of $\partial\Phi/\partial\sigma$ to be made using the nodal values of the potential at a series of nodes below the free surface.

In the following analysis, subscript 1 refers to the free surface node, and subscripts 2 and higher refer to subsequent nodes beneath the free surface node. Each value of σ is expressed as a multiple of the spacing $\Delta\sigma$ between the top two nodes.

$$\sigma_1 = 1 \quad \sigma_2 = 1 - \Delta\sigma \quad \sigma_3 = 1 - \alpha\,\Delta\sigma \quad \sigma_4 = 1 - \beta\Delta\sigma \tag{18}$$

If the vertical variation of the potential is assumed to be quadratic, then it can be written as

$$\Phi = A\left(\frac{\sigma - 1}{\Delta\sigma}\right)^2 + B\left(\frac{\sigma - 1}{\Delta\sigma}\right) + C \tag{19}$$

Putting in values for σ and Φ at three nodes (one on the free surface and two nodes vertically beneath) gives three simultaneous equations which can be solved for the unknown coefficients. Differentiating Equation (19) and using $\sigma_1 = 1$, gives the vertical gradient at the free surface as

$$\frac{\partial\Phi}{\partial\sigma} = \frac{2A(\sigma_1 - 1)}{\Delta\sigma^2} + \frac{B}{\Delta\sigma} = \frac{B}{\Delta\sigma} = \frac{(\alpha^2 - 1)\,\Phi_1 - \alpha^2\Phi_2 + \Phi_3}{\alpha(\alpha - 1)\,\Delta\sigma} \tag{20}$$

If the nodes are evenly spaced then $\alpha = 2$, leading to

$$\frac{\partial\Phi}{\partial\sigma} = \frac{3\Phi_1 - 4\Phi_2 + \Phi_3}{2\Delta\sigma} \tag{21}$$

A higher-order formula, assuming a quartic variation of Φ, and using five nodes, can be obtained by a similar procedure. For the case of evenly spaced nodes:

$$\frac{\partial\Phi}{\partial\sigma} = \frac{25\Phi_1 - 48\Phi_2 + 36\Phi_3 - 16\Phi_4 + 3\Phi_5}{12\Delta\sigma} \tag{22}$$

The horizontal and vertical velocities, u and w, can be found from these gradients using the following:

$$u = \frac{\partial\phi}{\partial x} = \frac{1}{l}\frac{\partial\Phi}{\partial X} + \frac{1}{lh}\left(-\sigma\,\frac{\partial\eta}{\partial X} + (1 - \sigma)\,\frac{\partial d}{\partial X}\right)\frac{\partial\Phi}{\partial\sigma} \tag{23}$$

$$w = \frac{\partial\phi}{\partial z} = \frac{1}{h}\,\frac{\partial\Phi}{\partial\sigma} \tag{24}$$

3.5. *Updating the free surface*

The velocity components are used to find the rates of change of the free surface elevation and free surface potential with time. The free surface kinematic boundary condition, Equation (4), yields:

$$\frac{\partial\eta}{\partial T} = w - u\,\frac{\partial\eta}{\partial x} = w - \frac{u}{l}\,\frac{\partial\eta}{\partial X} \tag{25}$$

The dynamic free surface boundary condition, Equation (3), becomes:

$$\frac{\partial\Phi}{\partial T} = -g\eta - \frac{1}{2}\,(u^2 + v^2) + \frac{\partial\eta}{\partial T}\,w \tag{26}$$

where use has been made of Equations (6) and (7). The term involving the rate of change of η is obtained from Equation (25).

The rates of change of free surface elevation and free surface potential are used to step these values forward in time, using a fourth-order Runge–Kutta scheme to obtain the non-linear motions of the free surface to a reasonable level of accuracy while retaining computational stability [9]. This is particularly important when modelling steep waves.

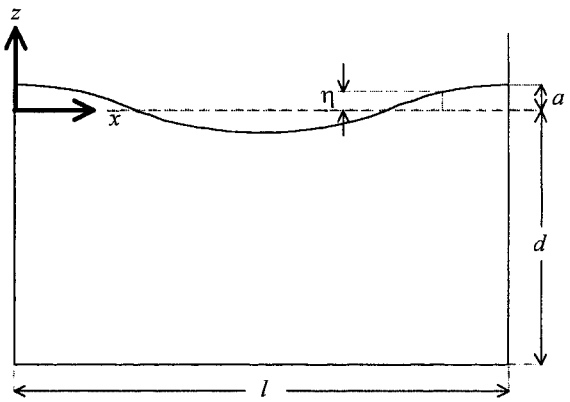

Figure 2. Initial free surface profile in a rectangular tank.

3.6. Smoothing for steep wave cases

When steep waves are simulated it is necessary to perform smoothing on the free surface in order to prevent the development of instabilities. This involves assigning new values to the nodal values of η and Φ based on a weighted average of the initially calculated nodal values. Two smoothing functions have been used, one based on five nodes (see Reference [5]):

$$\eta_i^* = \frac{1}{16}(-\eta_{i-2} + 4\eta_{i-1} + 10\eta_i + 4\eta_{i+1} - \eta_{i+2}) \tag{27}$$

and the other based on a template of seven nodes:

$$\eta_i^* = \frac{1}{32}(-\eta_{i-3} + 9\eta_{i-1} + 16\eta_i + 9\eta_{i+1} - \eta_{i+3}) \tag{28}$$

Similar formulas apply for Φ. For the test cases considered in this paper, smoothing was not required except for Stokes' progressive waves of steepness >0.3.

4. RESULTS

4.1. Free sloshing in a fixed rectangular tank

Figure 2 shows a fixed rectangular tank of length, l, and still water depth, d. The free surface is released from rest, with initial profile corresponding to a sinusoid given by

$$\eta = a\cos\left(\frac{2\pi x}{l}\right) \tag{29}$$

where a is the amplitude of the sinusoidal free surface profile, l is the wavelength, and x is the horizontal distance from the origin, which is located at the mean free surface position at the far left of the tank. The length to still water depth ratio, $l/d = 2$.

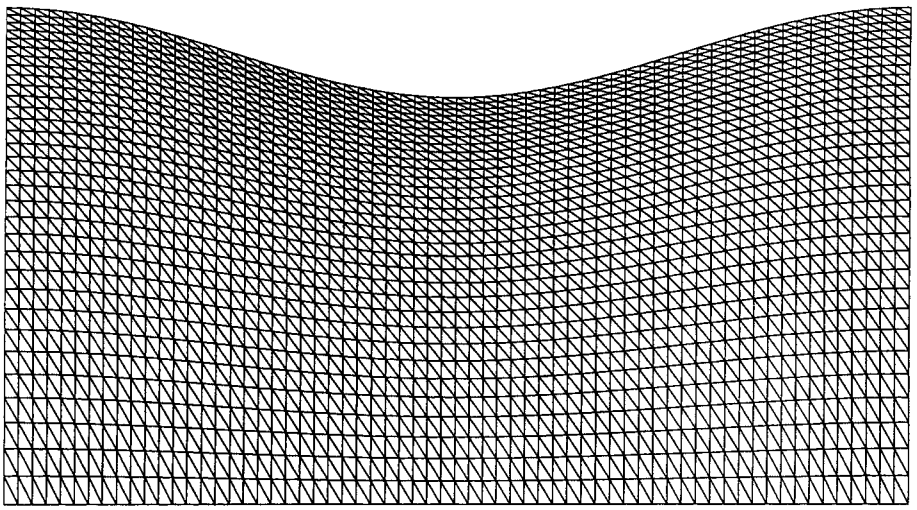

Figure 3. Initial 64×32 element mesh in physical domain; $a/d = 0.1$.

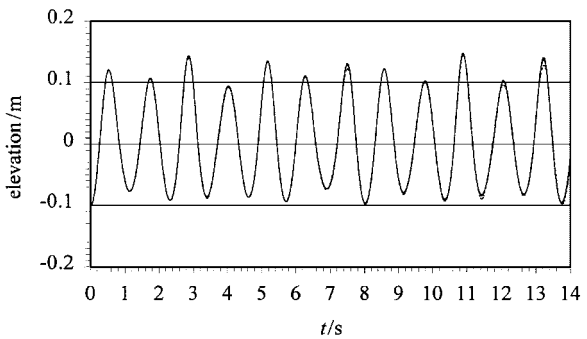

Figure 4. Mesh convergence tests for $a/d = 0.01$. Solid line: fine mesh (128×64); Long dashed line: intermediate mesh (64×32); Short dashed line: coarse mesh (32×16).

The mesh was chosen to be non-uniform in the transformed domain; in fact, the node spacing at the free surface was four times finer than at the base of the tank. The horizontal node spacing was uniform. Figure 3 illustrates an initial mesh in the physical domain consisting of 64 horizontal by 32 vertical elements. Here, the vertical and horizontal velocity components at the free surface were calculated using the higher-order calculation and least-squares method, respectively. Smoothing was not applied. Figure 4 depicts the free surface time history at the centre of the tank obtained using a fine mesh (128×64), intermediate mesh (64×32) and coarse mesh (32×16). The results obtained using the fine and intermediate meshes are almost identical, indicating that mesh convergence was achieved using a mesh of 64×32 elements. Similar stability tests for different time steps using the 64×32 element mesh indicated that $\Delta t = 0.05\sqrt{d/g}$ was sufficient; the CPU time per time step was 2.5 s on a 200 MHz Sun Workstation.

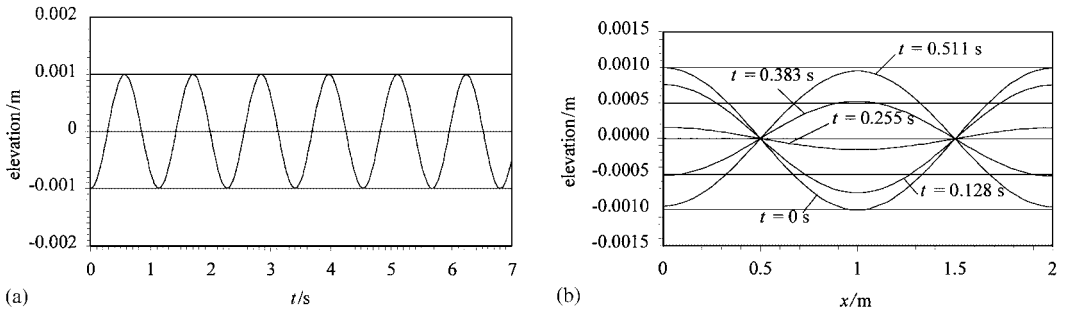

Figure 5. (a) Time history of the free surface elevation at the centre of the tank. Free sloshing with $a/d = 0.001$; Solid line: σ-transform solution; dashed line: linear solution. (b) Spatial profiles at different times during the oscillation. Free sloshing with $a/d = 0.001$. σ-transform solution.

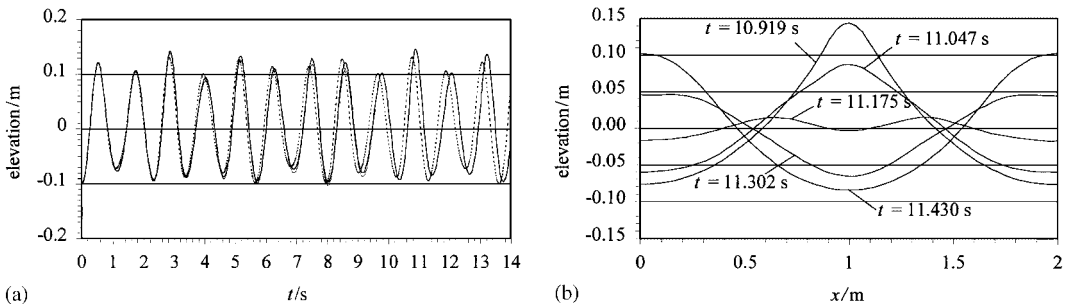

Figure 6. (a) Time history of the free surface elevation at the centre of the tank. Free sloshing with $a/d = 0.1$. Solid line: σ-transform solution; dashed line: second-order solution; thin line: solution of Chern *et al.* [16]. (b) Space profiles at different times during the oscillation. Free sloshing with $a/d = 0.1$. σ-transform solution.

For $a/d = 0.001$, the small amplitude oscillations were almost perfectly sinusoidal, in accordance with linear potential theory. Figure 5(a) presents the time-dependent behaviour of the free surface at the centre of the tank, along with the analytical solution from first-order potential theory, which is

$$\eta_1 = -a\cos(\omega_2 t) \tag{30}$$

where $\omega_2 = \sqrt{gk_2\tanh(k_2 d)}$ and $k_2 = 2\pi/l$. The numerical and analytical results are virtually identical, and there is no discernible phase difference. Spatial profiles of the free surface along the tank at intervals during a typical sloshing wave period are shown in Figure 5(b), where a pair of nodes occur exactly at $x/l = 0.25$ and 0.75. The profiles are sinusoidal and repeatable, confirming that the small amplitude sloshing is linear.

For $a/d = 0.1$, the sloshing amplitude is large, and the waves are steep and non-linear. The same mesh and time step were used as before. Figure 6(a) depicts the free surface motions at the centre of the tank. Superimposed on Figure 6(a) are the numerical results from Chern

et al. [16] who used a pseudospectral approach and the analytical solution from second-order potential theory [9]. The latter can be expressed as

$$\eta_2 = -a\cos(\omega_2 t) + \frac{1}{8g}\left(2(\omega_2 a)^2\cos(2\omega_2 t) + \frac{a^2}{\omega_2^2}(g^2k_2^2 + \omega_2^4)\right.$$
$$\left. - \frac{a^2}{\omega_2^2}(g^2k_2^2 + 3\omega_2^4)\cos(\omega_4 t)\right) \tag{31}$$

where $\omega_4 = \sqrt{gk_4\tanh(k_4 d)}$ and $k_4 = 4\pi/l$. The σ-transformed finite element and pseudospectral models give results that almost overlay each other, and are very similar to those obtained by Greaves *et al.* [24] who used a finite element potential flow model based on triangularised quadtree meshes. The numerical results are in close agreement with the second-order analytical solution except for a phase difference. This difference is due to high-order non-linearities (third and above) that alter the fundamental oscillation frequency: in this case one can estimate from Figure 6(a) that $\omega/\omega_0 = 0.990$ where ω_0 is the sloshing frequency predicted by linear wave theory. When the amplitude ratio, a/d, is increased to 0.13, the estimated ratio ω/ω_0 is 0.982. This is similar to the value $\omega/\omega_0 = 0.978$ found by Greaves *et al.* [24] for $a/d = 0.13$. Moreover, Tsai and Jeng [25] obtained $\omega/\omega_0 = 0.979$ for $a/d = 0.13$ by replacing the velocity potential by a truncated Fourier series and solving Laplace's equation by Newton iteration.

Examination of the free surface time histories leads to the conclusion that in all cases the first and second peaks coincide with the second-order solution, but the third peak is appreciably larger and the fourth smaller. The first trough is deeper, the second shallower, the third similar and the fourth deeper. Figure 6(b) illustrates the spatial behaviour of the free surface along the tank at intervals over a sloshing period, for the case $a/d = 0.1$. At the centre of the tank, the wave peak is higher and narrower and the trough shallower and wider than for the small amplitude case. As also observed by Chern *et al.* [16], the well defined nodes one-quarter and three-quarters along the tank obtained for linear sloshing have disappeared; instead the surface profiles are much more complicated due to non-linearity.

Figure 7 compares the free surface elevation time histories at the centre of the tank obtained using higher order velocity and least squares velocity calculations described previously. The higher order velocity calculations are without smoothing, unlike the least squares calculations, which broke down if smoothing was not implemented.

4.2. Forced sloshing in a base-excited rectangular tank

Sloshing wave motion can be generated in a rectangular tank by oscillating the entire tank horizontally. For small amplitudes this is equivalent to imposing the same horizontal velocity on both the side walls. If the frequency of this imposed motion is similar to the natural sloshing frequency then resonance will occur.

For all simulations in this section, a structured mesh is used of 64×32 elements ($l/d = 2$) and the time step is $0.1\sqrt{d/g}$; the CPU time per time step on the Sun Workstation is 2.5 s. The initial free surface elevation is everywhere zero. The velocity of the side walls is given by $u = a\omega\sin(\omega t)$ where ω is the frequency of oscillation and a is the effective amplitude of oscillation of the side walls.

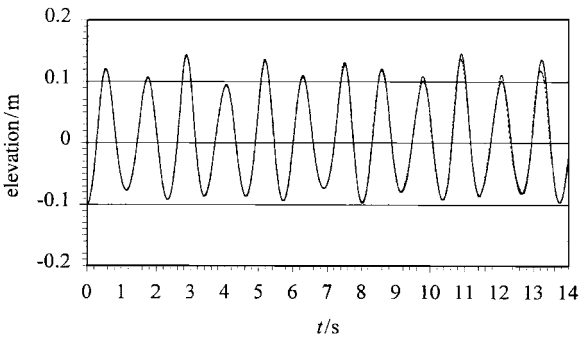

Figure 7. Comparison between velocity calculation methods, $a/d = 0.1$. Solid line: higher order velocity calculation without smoothing; Dashed line: least squares velocity calculation with smoothing.

The linear solution for the free surface elevation [11] is

$$\eta = \eta_1 + \eta_2 \tag{32}$$

where

$$\eta_1 = \frac{a}{g}\left(x\omega^2 + \sum_{n=0}^{\infty} C_n\omega \sin(k_n x)\right)\sin(\omega t) \tag{33}$$

$$\eta_2 = -\frac{a}{g}\sum_{n=0}^{\infty} \omega_n\left(C_n + \frac{H_n}{\omega^2}\right)\sin(k_n x)\sin(\omega_n t) \tag{34}$$

and

$$k_n = \frac{(2n+1)\pi}{l}, \quad \omega_n = (gk_n \tanh(k_n d))^{1/2}, \quad H_n = \frac{(-1)^n 4\omega^3}{bk_n^2}, \quad C_n = \frac{H_n}{\omega_n^2 - \omega^2} \tag{35}$$

Using the above equations, the natural sloshing frequency is $\omega_0 = 1.2\sqrt{g/d}$.

Figure 8 displays the time history of the free surface elevation at the left-hand wall of the tank, for an excitation frequency $\omega = 0.999\omega_0$. In this case, the oscillation amplitude monotonically increases with time. When the excitation frequency is increased to $1.1\omega_0$, the free surface elevation given in Figure 9 is quite different in that it is modulated and repeatable. Predictions by the present model are in close agreement with the corresponding linear analytical solutions given by Equation (32) and the predictions by Chern *et al.*'s [16] pseudospectral model, also shown in Figures 8 and 9.

4.3. Regular progressive waves due to a wave-maker

Progressive free surface waves were generated in the numerical flume illustrated in Figure 10, by imposing the horizontal water particle velocity component, u, (as predicted by linear theory) as a boundary condition on the lateral wall at the left-hand end of the flume. Thus

$$u = \frac{H\omega}{2}\frac{\cosh(k(d+z))}{\sinh(kd)}\cos(\omega t) \tag{36}$$

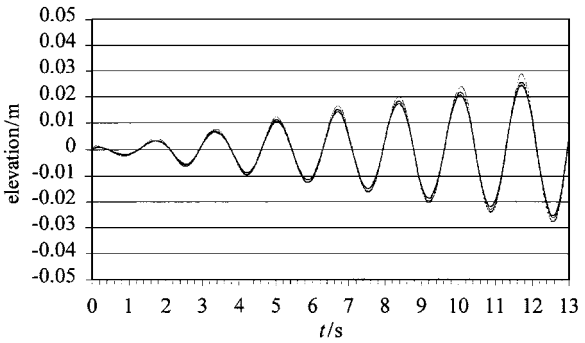

Figure 8. Time history of free surface elevation at left wall of a base-excited tank. Excitation frequency, $\omega = 0.999\omega_0$. Solid line: σ-transform solution; dashed line: linear analytical solution; thin line: solution of Chern *et al.* [16].

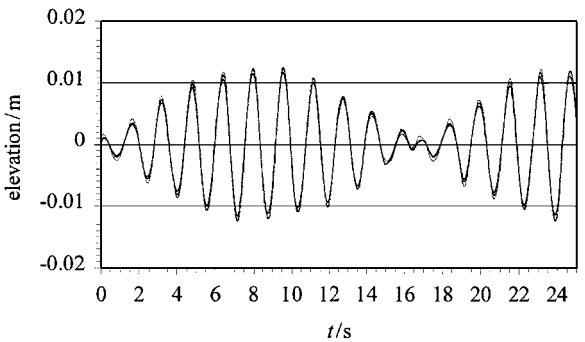

Figure 9. Time history of free surface elevation at left wall of base-excited tank. Excitation frequency, $\omega = 1.1\omega_0$. Solid line: σ-transform solution; dashed line: linear analytical solution; thin line: solution of Chern *et al.* [16].

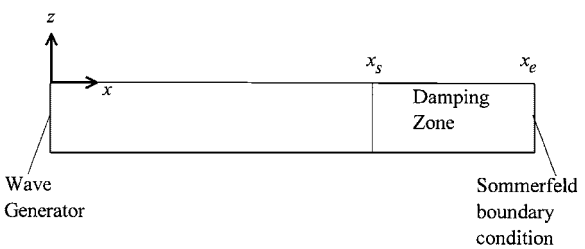

Figure 10. Wave tank for progressive wave case.

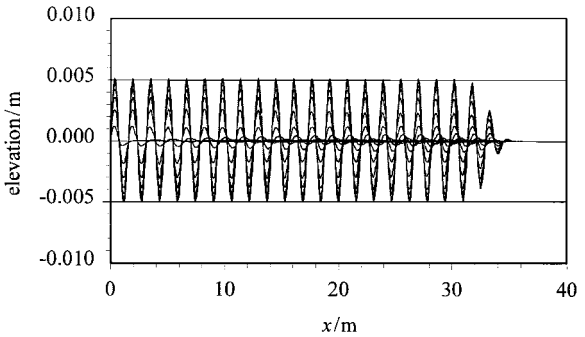

Figure 11. Spatial profiles for $t = 0$ to $60\,T$ at intervals of $2T$. $H = 0.01$ m, $\omega = 6.264$ rad/s.

where H is the wave height, ω the angular wave frequency, k the wave number magnitude, d the still water depth, z the vertical distance above still water level, and t the time. At the right-hand end of the tank, wave absorption was achieved using the Sommerfeld radiation criterion in conjunction with a damping layer. The Sommerfeld radiation condition is $\partial\phi/\partial t = -c\partial\phi/\partial x$ where c is the wave celerity determined from linear theory. The damping layer is implemented by modifying the time derivatives of the free surface elevation and surface velocity potential, such that in the transformed domain

$$\frac{\partial \eta}{\partial T} = \frac{\partial \eta_p}{\partial T} - S\omega\left(\frac{X - X_s}{X_e - X_s}\right)^3 \eta_p \quad \text{and} \quad \frac{\partial \Phi}{\partial T} = \frac{\partial \Phi_p}{\partial T} - S\omega\left(\frac{X - X_s}{X_e - X_s}\right)^3 \Phi_p \tag{37}$$

where X_s and X_e are the X-co-ordinates of the beginning and end of the damping layer, the subscript p denotes the value predicted by the numerical model, and S is a prescribed coefficient. For the cases considered herein, $S = 3$ was found to give satisfactory results.

The numerical wave tank was of length 40 m and contained water of still water depth 1 m. The damping layer was 10 m long. Results were obtained for progressive waves of period $T = 1.003$ s (or angular frequency $\omega = 6.264$ rad/s), corresponding to a non-dimensional period $\hat{T} = T\sqrt{g/d} = \pi$ (or non-dimensional frequency $\hat{\omega} = 2$). Using the linear dispersion equation, one can show that the corresponding (linear) wavelength is 1.5708 m, the wave number $k = 4$ rad/m and the celerity $c = 1.5661$ m/s. Here, $kd = 4$ and the case corresponds to deep water waves. Mesh convergence was achieved using a 640 horizontal by 16 vertical element σ-transformed mesh. Stable and accurate results were obtained using a time step of $\Delta t = T/20 = 0.05015$ s, requiring a CPU time of 16 s per time step. Free surface smoothing was only applied for the steepest wave cases. An initial ramp function was applied to the wave-maker velocity in order to prevent spurious oscillations from developing, namely $u_R = u\tanh(t/6.3855)$. The damping layer was applied to the free surface from $x_s = 30$ m to $x_e = 40$ m. Figure 11 shows the evolution of small amplitude waves generated when the paddle velocity has amplitude, $U_o = H\omega/2 = 0.03132$ m/s, corresponding to a linear theory wave height of 0.01 m. Spatial profiles are plotted along the tank at intervals equal to twice the wave period for $t = 0$ to $60T$. At any given location between the wave-maker and damping layer, the wave amplitude grows until it reaches a steady value equal to 0.005 m, in agreement with linear theory. Figure 12 plots the time history of the free surface at the centre of the flume, where the initial amplitude growth is smooth due to the ramp function.

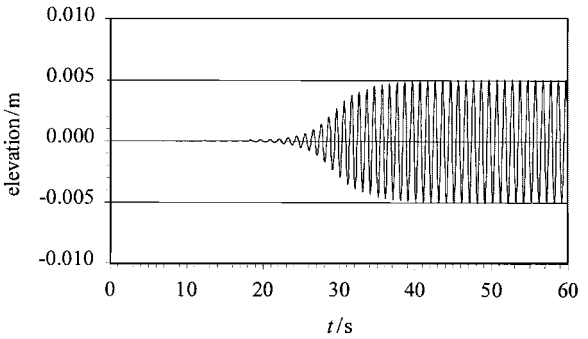

Figure 12. Time history at $x = 20$ m. $H = 0.01$ m, $\omega = 6.264$ rad/s.

The σ-transformed finite element model was then used to simulate large amplitude waves of appreciable non-linearity. The results were compared with Stokes' fifth-order wave theory as derived by Fenton [26], in which for deep water the free surface elevation is given by

$$\eta(x,t) = a_1 \cos(k(x-ct)) + a_2 \cos(2k(x-ct)) + a_3 \cos(3k(x-ct)) + a_4 \cos(4k(x-ct)) + a_5 \cos(5k(x-ct)) \tag{38}$$

where

$$a_1 = \frac{1}{k}\left(\varepsilon - \frac{3}{8}\varepsilon^3 - \frac{211}{192}\varepsilon^5\right)$$

$$a_2 = \frac{1}{k}\left(\frac{1}{2}\varepsilon^2 + \frac{1}{3}\varepsilon^4\right)$$

$$a_3 = \frac{1}{k}\left(\frac{3}{8}\varepsilon^3 + \frac{99}{128}\varepsilon^5\right)$$

$$a_4 = \frac{\varepsilon^4}{3k}$$

and $$a_5 = \frac{125\varepsilon^5}{384k}$$

for a wave steepness $\varepsilon = kH/2$, and a fundamental wave number, k, found from the solution of the equation

$$1 + \frac{\varepsilon^2}{2} + \frac{\varepsilon^4}{8} = \frac{\omega}{\sqrt{gk}} \tag{39}$$

Twelve simulations were performed, with the input linear wave height ranging from 0.025 to 0.3 m (corresponding to wave-maker velocity amplitudes ranging from 0.3915 to 0.9396 m/s). For each simulation, a portion of the steady state surface profile occupying 5 wavelengths has

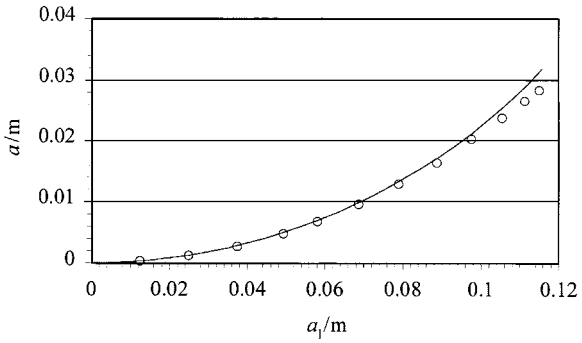

Figure 13. Plot of Fourier components a_2 against a_1. Circles: σ-transform; solid line: Stokes' fifth-order theory.

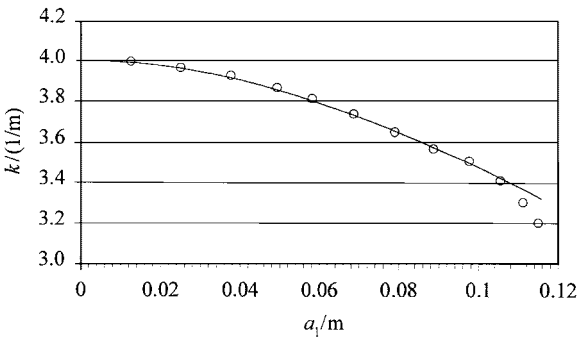

Figure 14. Wavenumber, k against Fourier component a_1. Circles: σ-transform; solid line: Stokes' fifth-order theory.

been analysed using the FFT toolbox in MATLAB, to obtain the Fourier components a_1 and a_2, corresponding to the wavelength and half the wavelength. These components are plotted against each other in Figure 13, together with those given by Stokes' fifth-order theory. It can be seen that there is a close match between the numerical and analytical predictions up to a first-component free surface elevation value of 0.06 m. Figure 14 presents the wave number as a function of the first Fourier component of free surface elevation. The wave number decreases as the first-order component (i.e. wave amplitude) increases, as would be expected due to the corresponding increase in wavelength. Again, there is excellent agreement between the wave tank and analytical results for first-component free surface elevation up to the near-breaking value of 0.09 m.

Figures 15 and 16 depict enlarged spatial profiles of the free surface for progressive waves of input linear wave height 0.225 and 0.3 m, respectively. In both cases, the numerical predictions differ from the analytical solution of Stokes' fifth order wave theory close to the driving boundary at $x = 0$ due to local transient free surface effects that appear to decay within a wavelength. Once established, the numerically predicted waves in Figure 15 have wave height 0.21 m, wavelength 1.79 m, and steepness $\varepsilon = 0.37$, and the profile is almost

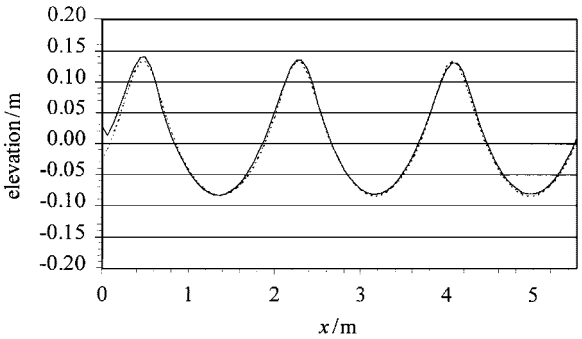

Figure 15. Input linear wave height, $H = 0.225$ m. Free surface elevation spatial profile. Solid line: σ-transform solution; dashed line: Stokes' fifth-order theory.

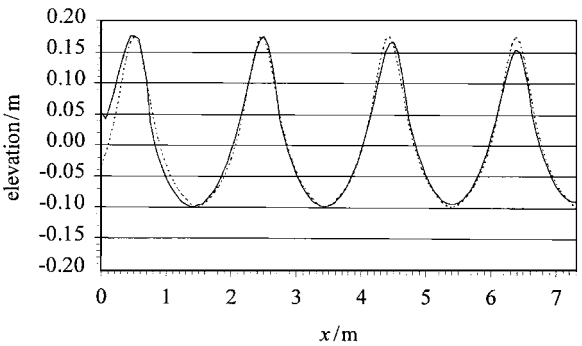

Figure 16. Input linear wave height, $H = 0.3$ m. Free surface elevation spatial profile. Solid line: σ-transform solution; dashed line: Stokes' fifth-order theory.

identical to that obtained from Stokes' fifth theory. Non-linear effects are evident, with the narrower taller crests and longer shallower troughs than would be expected from linear theory. In Figure 16, the established simulated waves have height 0.27 m and wavelength 1.957 m. The steepness is 0.43, and is equivalent to an almost-breaking wave. The agreement with Stokes' fifth theory is not so close as for the lower steepness case, and asymmetry is evident at the wave crest evaluated by the numerical method. The foregoing results verify that the σ-transformed finite element model is appropriate for simulating steep progressive waves.

The numerical wave tank was also used to simulate higher order shallow water waves. Driving wave boundary conditions in the numerical model consisted of time-dependent water particle velocities at the paddle corresponding to a wave height of 1.2192 m, wave period of 15.0 s, and mean water depth of 7.62 m in a tank of length 1528 m. The time step was 0.1875 s, and the mesh contained 2560×16 elements. The paddle motions were ramped up to limit cycle conditions according to a hyperbolic tangent formula. Figures 17 and 18 indicate that the predicted regular shallow water wave profiles in space and time are in very close agreement with analytical solutions from second-order cnoidal wave theory [27].

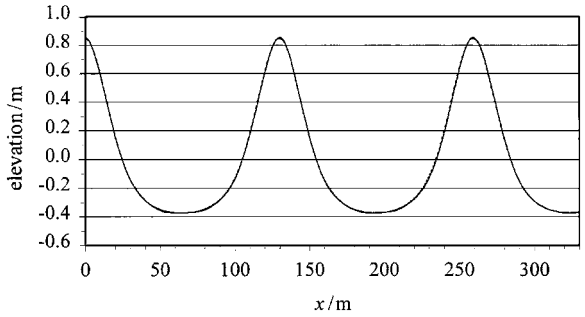

Figure 17. Cnoidal wave. Wave height = 1.2192 m. Period = 15 s. Free surface elevation spatial profile. Solid line: σ-transform solution; dashed line: cnoidal second-order theory.

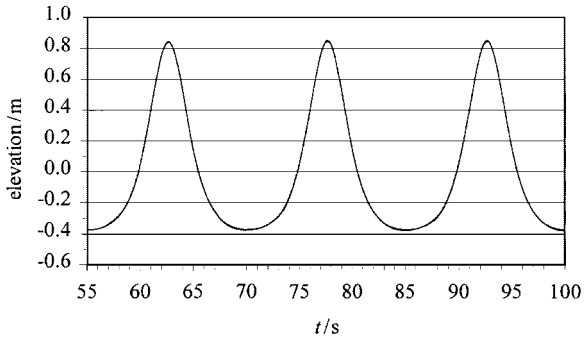

Figure 18. Cnoidal wave. Wave height = 1.2192 m. Period = 15 s. Free surface elevation time history. Solid line: σ-transform solution; dashed line: cnoidal second-order theory.

4.4. Focused wave

In recent years, the concept of a focused wave group has been used to represent the profile of the extreme wave, whereby all wave components in a deepwater sea spectrum focus simultaneously at a point in space. Tromans *et al.* [28], Jonathan *et al.* [29] and Taylor and Haagsma [30] developed NewWave theory based on the focused wave idea, which has been incorporated into a design calculation methodology for offshore structures. In particular, Tromans *et al.* found that the profile of a linear focused wave group is directly proportional to the auto-correlation function of the spectrum. Baldock *et al.* [31] conducted meticulous experimental investigations into the free surface motions and underlying kinematics of focused wave groups in deep water. Baldock *et al.* examined the effect of non-linearity on focused wave group in a unidirectional wave flume, and compared their experimental data with linear and second-order theory. In this paper, the σ-transformed finite-element model is used to simulate Cases B and D that were measured by Baldock *et al.* in the flume.

The focused wave produced by Baldock *et al.* [31] has free surface elevation at the paddle given by

$$\eta(x_p, t) = \sum_{n=1}^{N} a_n \cos(k_n x_p + \omega_n t) \tag{40}$$

where a_n, k_n, and ω_n are, respectively, the amplitude, wave number and wave frequency of the nth wave component, N is the total number of wave components, x_p is the distance from the paddle to the linear focus position, and t is time. The corresponding paddle velocity profile in the numerical wave tank is given by

$$u(x_p, z, t) = \sum_{n=1}^{N} a_n \omega_n \frac{\cosh(k_n(d+z))}{\sinh(k_n d)} \cos(k_n x_p + \omega_n t) \tag{41}$$

where d is the still water depth and z is the vertical distance above still water level. The wave amplitude at the focus point is $A = \sum_{n=1}^{N} a_n$ according to linear theory.

The experimental tank used by Baldock *et al.* was 20 m long, 0.3 m wide and had a depth of 0.7 m. The numerical tank used here has a depth of 0.7 m, and is 28 m long, with a 7 m damping zone at the far end. The computational mesh is 1280 elements long and 16 elements deep. The time step is 0.021 s. Smoothing is not applied. The CPU time was 31 s per time step on the Sun Workstation.

We consider results for two cases considered by Baldock *et al.*, for spectra where each component is of equal amplitude and equally spaced in the period domain. The first, Case B, relates to a relatively broad-band spectrum where the periods range from 0.6 to 1.4 s. The second, Case D, corresponds to a narrow-band spectrum where the periods range from 0.8 to 1.2 s.

Figures 19 and 20 depict the time-dependent free surface motions at the focal point for Cases B and D, respectively. The finite element model predictions (solid lines) and experimental measurements (dotted lines) match closely over the range of focus wave group amplitudes considered. The linear solution is also plotted (dashed line), and, although excellent agreement is obtained for the lower amplitude focused wave group, the effect of non-linearity at higher amplitude leads to under-prediction of the maximum crest elevation and over-estimation of the trough. This is in keeping with Baldock *et al.* who found that second-order theory gave better predictions than linear theory for focused wave groups. It should be noted that Johannessen and Swan [32] have simulated the same cases and obtained very similar results using an extension of Fenton and Rienecker's [33] non-linear wave propagation model.

The maximum crest elevation is plotted against input amplitude (i.e. the linear wave focused wave amplitude) for Cases B and D in Figure 21. Excellent agreement is achieved between the numerical predictions and Baldock *et al.*'s measurements. The non-linear growth in maximum crest elevation with input amplitude is greater for the narrow-band spectrum, Case D, than for broad-band Case B (again in keeping with Baldock *et al.*).

5. CONCLUSIONS

Details have been presented of a numerical wave tank based on a σ-transformed finite element solution of Laplace's equation for irrotational flow, with fully non-linear free

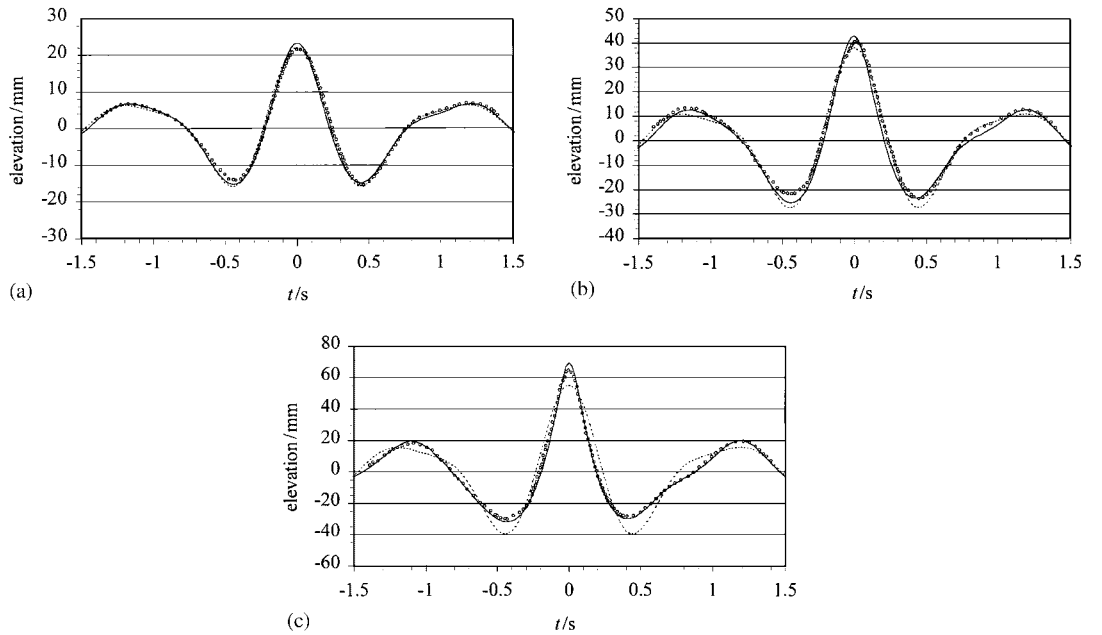

Figure 19. (a) Case B. $A = 22$ mm. Time history of free surface elevation at the focal point. Solid line: σ-transform; dashed line: linear solution; points: Baldock *et al.* [31]. (b) Case B. $A = 38$ mm. Time history of free surface elevation at the focal point. Solid line: σ-transform; dashed line: linear solution; points: Baldock *et al.* [31]. (c) Case B. $A = 55$ mm. Time history of free surface elevation at the focal point. Solid line: σ-transform; dashed line: linear solution; points: Baldock *et al.* [31].

surface dynamic and kinematic boundary conditions. The use of the σ-transformation has two main advantages. First, there is no need for remeshing in the computational domain, the free surface motions being accounted for by means of extra complexity of the mathematical formulation. Second, as a consequence, the vertical component of surface velocity can be calculated using a high-order technique. This removes the need for free surface smoothing, except for very steep waves. The method is applicable to inviscid free surface motions of incompressible liquids, provided the motions are not so violent that incipient overturning conditions are reached where the free surface becomes vertical and the mapping ceases to be unique.

The numerical model has been used to simulate non-linear free surface sloshing in fixed and horizontally excited rectangular tanks, and the results found to match closely those from alternative numerical schemes. Excellent agreement is achieved with linear and second-order potential theory for small amplitude motions. At larger amplitudes, the effect of non-linearities becomes increasingly evident and the numerical predictions differ from the low order theory.

For progressive regular waves in a flume, close agreement is achieved with Stokes' fifth-order theory for waves almost up to breaking, and with second-order cnoidal wave theory in shallow water. Simulations of focused wave groups are also in excellent agreement with experimental data provided by Baldock *et al.* [31].

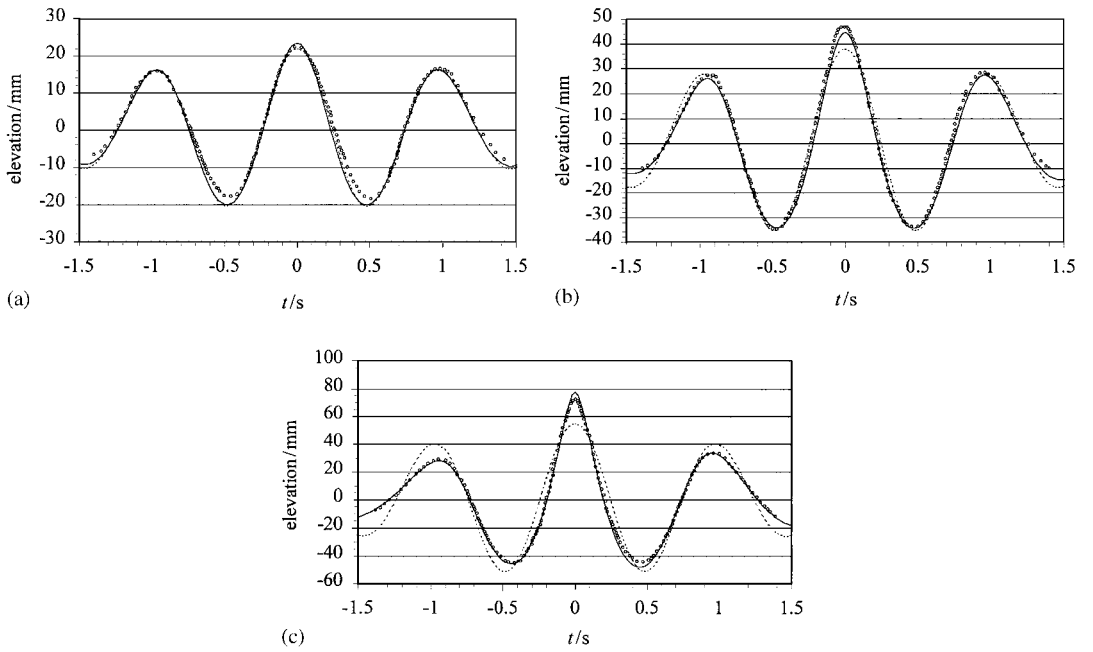

Figure 20. (a) Case D. $A = 22$ mm. Time history of free surface elevation at the focal point. Solid line: σ-transform; dashed line: linear solution; points: Baldock *et al.* [31]. (b) Case D. $A = 38$ mm. Time history of free surface elevation at the focal point. Solid line: σ-transform; dashed line: linear solution; points: Baldock *et al.* [31]. (c) Case D. $A = 55$ mm. Time history of free surface elevation at the focal point. Solid line: σ-transform; dashed line: linear solution. points: Baldock *et al.* [31].

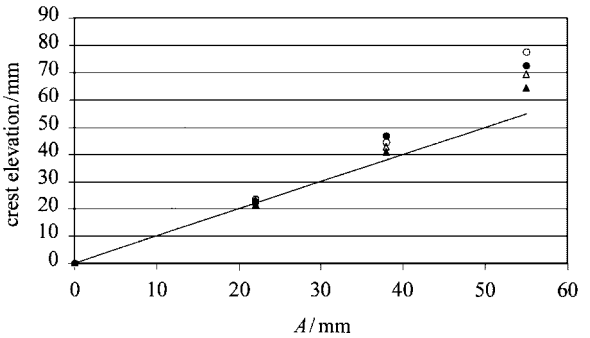

Figure 21. Crest elevations. White triangle : sigma case B; white circle : sigma case D; black triangle : Baldock *et al.* [31] case B; black circle : Baldock *et al.* [31] case D; solid line : linear solution.

ACKNOWLEDGEMENTS

The authors gratefully acknowledge the financial support provided by the Engineering and Physical Sciences Research Council (EPSRC) Grant GR/M 56401. The authors would also like to thank Dr Paul Taylor for advice on the steep progressive and focused wave cases, Professor GX Wu for the original finite element code and Dr M-J Chern for supplying data for comparison.

REFERENCES

1. Grue J, Bjorshol G, Strand O. Higher harmonic wave exciting forces on a vertical cylinder. *Institute of Mathematics*, University of Oslo Preprint, No. 2. ISBN 82-553-0862-8, 1993.
2. Faltinsen OM, Newman JN, Vinje T. Non-linear wave loads on a slender vertical cylinder. *Journal of Fluid Mechanics* 1995; **289**:179–198.
3. Stansberg CT, Huse E, Krokstad JR, Lehn E. Experimental study of non-linear loads on vertical cylinders in steep random waves. *Proceedings of the Fifth International Offshore and Polar Engineering Conference*, vol. 1, 1995; 75–82.
4. Chaplin JR, Rainey RCT, Yemm RW. Ringing of a vertical cylinder in waves. *Journal of Fluid Mechanics* 1997; **350**:119–147.
5. Longuet-Higgins MS, Cokelet ED. The deformation of steep surface waves on water, I: a numerical method of computation. *Proceedings of the Royal Society of London*, *Series A* 1976; **350**:1–25.
6. Kim CH, Clement AH, Tanizawa K. Recent research and development of numerical wave tanks—a review. *International Journal of Offshore and Polar Engineering* 1999; **9**:241–256.
7. Ferrant P. Run up on a cylinder due to waves and current: potential flow solution with fully non-linear boundary conditions. *International Journal of Offshore and Polar Engineering* 2001; **11**:33–41.
8. Boo SY. Linear and non-linear irregular waves and forces in a numerical wave tank. *Ocean Engineering*. 2002; **29**: 475–493.
9. Wu GX, Eatock Taylor R. Finite element analysis of two-dimensional non-linear transient water waves. *Applied Ocean Research* 1994; **16**:363–372.
10. Wu GX, Eatock Taylor R. Time stepping solutions of the two dimensional non-linear wave radiation problem. *Ocean Engineering*. 1995; **22**(8):785–798.
11. Wu GX, Ma QW, Eatock Taylor R. Numerical simulation of sloshing waves in a 3D tank based on a finite element method. *Applied Ocean Research* 1998; **20**:337–355.
12. Ma QW, Wu GX, Eatock Taylor R. Finite element simulation of fully non-linear interaction between vertical cylinders and steep waves—part 1: methodology and numerical procedure. *International Journal for Numerical Methods in Fluids* 2001; **36**:265–285.
13. Ma QW, Wu GX, Eatock Taylor R. Finite element simulation of fully non-linear interaction between vertical cylinders and steep waves, part 2: numerical results and validation. *International Journal for Numerical Methods in Fluids* 2001; **36**:287–308.
14. Nestegard A. Status of non-linear hydrodynamic modelling. *Technical Report*, *DNV*, Norway, 1999.
15. Robertson I, Sherwin S. Free-surface flow simulation using hp/spectral elements. *Journal of Computational Physics* 1999; **155**:26–53.
16. Chern MJ, Borthwick AGL, Eatock Taylor R. A pseudospectral σ-transformation model of 2-D non-linear waves. *Journal of Fluids and Structures* 1999; **13**:607–630.
17. Chern MJ, Borthwick AGL, Eatock Taylor R. Simulation of non-linear free surface motions in a cylindrical domain using a Chebyshev-Fourier spectral collocation method. *International Journal for Numerical Methods in Fluids* 2001; **36**:465–496.
18. Le Touze D, Bonnetoy F, Ferrant P. Second order spectral simulation of directional waves generation and propagation in a 3D tank. *Proceedings of the 12th International Offshore and Polar Engineering Conference*, 2002.
19. Wu GX, Eatock Taylor R. The coupled finite element and boundary element analysis of non-linear interactions between waves and bodies. *Ocean Engineering* 2003; **30**:387–400.
20. Stelling GS, van Kester JATHM. On the approximation of horizontal gradients in sigma co-ordinates for bathymetry with steep bottom slopes. *International Journal for Numerical Methods in Fluids* 1994; **18**: 915–935.
21. Huang W, Spaulding M. 3D model of estuarine circulation and water quality induced by surface discharges. *ASCE Journal of Hydraulic Engineering* 1995; **21**(4):300–311.
22. Koçyigit MB, Falconer RA, Lin B. Three-dimensional numerical modelling of free surface flows with non-hydrostatic pressure. *International Journal for Numerical Methods in Fluids* 2002; **40**(9):1145–1162.
23. Eatock Taylor R, Borthwick AGL, Greaves DM, Wu GX, Ma QW. EPSRC/MTD Managed Programme on Uncertainties in Loads on Offshore Structures. *Project technical report. Project A3*: *Interaction of steep waves with structures*, 1996.
24. Greaves DM, Borthwick AGL, Wu GX, Eatock Taylor R. A moving boundary finite element method for fully non-linear wave simulations. *Journal of Ship Research* 1997; **41**(3):181–194.
25. Tsai CP, Jeng DS. Numerical Fourier solutions of standing waves in finite water depth. *Applied Ocean Research* 1994; **16**:185–193.
26. Fenton JD. A fifth-order Stokes theory for steady waves. *Journal of Waterway, Port Coastal and Ocean Engineering*, *ASCE* 1985; **111**:216–234.
27. Sarpkaya T, Isaacson M. *Mechanics of Wave Forces on Offshore Structures*. Van Nostrand Reinhold: New York, 1981.

28. Tromans PS, Anaturk AR, Hagemeijer P. A new model for the kinematics of large ocean waves—application as a design wave. *Proceedings of the 1st International Offshore and Polar Engineering Conference*, Edinburgh, U.K., 11–16 August, 1991; 64–71.
29. Jonathan P, Taylor PH, Tromans PS. Storm waves in the northern North Sea. *Proceedings of the 7th International Conference on the Behaviour of Offshore Structures* (*BOSS*), vol. 2, 1994; 481–494.
30. Taylor PH, Haagsma IJ. Focussing of steep wave groups on deep water. *Proceedings of the International Symposium*: *Waves—Physical and Numerical Modelling*, Vancouver, Canada, 21–24 August, 1994; 862–870.
31. Baldock TE, Swan C, Taylor PH. A laboratory study of non-linear surface waves on water. *Philosophical Transactions of the Royal Society of London*, *Series A* 1996; **354**:649–676.
32. Johannessen TB, Swan PH. Non-linear transient water waves—part I. A numerical method of computation with comparisons to 2-D laboratory data. *Applied Ocean Research* 1997; **19**:293–308.
33. Fenton JD, Rienecker MM. Accurate numerical solutions for non-linear waves. In *7th International Conference on Coastal Engineering*, vol. 1, Sydney, Australia, 1980; 50–69.

